

A Multiscale Calibration of a Photon Videomicroscope for Visual Servo Control: Application to MEMS Micromanipulation and Microassembly

Brahim TAMADAZTE, Soukalo DEMBÉLÉ and Nadine PIAT

FEMTO-ST Institute/AS2M, UMR CNRS 6174 - UFC / ENSMM / UTBM,

24 rue Alain Savary, 25000 Besançon, France

Tel.: +33 (0)3 81 40 27 99, fax: +33 (0)3 81 40 28 09

E-mail: {btamadaz, sdembele, npiat}@ens2m.fr

Received: 29 January 2009 /Accepted: 23 February 2009 /Published: 23 March 2009

Abstract: For many years, the increasing development of microcomponents based products requires more and more microassembly systems to permit the assembly of micrometric parts and MEMS. These systems require different tasks such as micromanipulation, microassembly, supervision, quality inspection and also require accurate metric measurements from images. The most widely used image sensor is the photon videomicroscope which is characterized by several weaknesses such as the depth-of-field and the field-of-view. This paper deals with the calibration of this kind of imaging system used for robotic microassembly. In the first part, a multiscale calibration paradigm is proposed and is used to *pick and place* silicon microparts ($400 \times 400 \times 100 \mu\text{m}^3$) using multiscale 2D visual servoing. In a second part, these microparts are assembled by a 3D visual control approach. High precision, repeatable results are obtained during the MEMS manipulation and assembly tasks. Copyright © 2009 IFSA.

Keywords: microscope calibration, image-based and pose-based visual control, MEMS, robotic micromanipulation and microassembly.

1. Introduction

As compared with macroscopic and mesoscopic scales where assembly can be achieved without vision feedback, manipulation at microscopic scale always requires images. The manipulation of biological objects (pollen or living cells) is a typical example of micromanipulation. However, for many years the manipulation of artificial objects such as monolithic microcomponents, MEMS (Micro-Electro-

Mechanical-System) and MOEMS (Micro-Opto-Electro-Mechanical-System) has also emerged. In this case, the images represent the views of the work scene from which metric information can be derived (e.g. the pose of a component or a gripper, the distance between a component and a gripper, the speed of a gripper). This data is required for the 2D or 3D reconstruction of the scene and the quality inspection or the control of manipulators. Microassembly corresponds to the assembly task at the microscale, and implies the manipulation of components with a size between $1\ \mu\text{m}$ and $1\ \text{mm}$ and an accuracy range of $1\ \mu\text{m}$ [1, 2]. A vision system well-adapted to this range is the optical (photonic) microscope equipped with high magnification lenses. This type of imaging system offers a very high resolution that reaches $0.2\ \mu\text{m}$. Unfortunately it has also two important drawbacks which are the weakness of the field-of-view and the depth-of-field. For the system used in the experiments presented below (*Leica MZI6A*), the field-of-view is $700\ \mu\text{m} \times 900\ \mu\text{m}$ at the maximum of the zoom; the depth-of-field varies between $2.9\ \text{mm}$ and $0.035\ \text{mm}$ according to the numerical aperture of the objective. These characteristics complicate greatly the calibration and limit the use of the videomicroscope.

This paper deals with the issues of modeling and calibration of the motor zoom photon videomicroscope and the micromanipulation and microassembly of MEMS using vision feedback control. Few solutions have been proposed in the literature for the optical microscope calibration. The most known is the one of Zhou *et al.* [3]. The authors point out the differences between a standard image source (with a standard video lens) and a videomicroscope. They model the latter by the usual perspective non-linear model in which the optical tube length (T_{op}) is introduced in the equations. The parameters of their model are T_{op} , f , d and k_l , where parameter f is the focal length, d is the distance between the object plane and the front focal plane and k_l is the lens radial distortion. The calibration algorithm developed by Tsai [4] is used to compute the above parameters and the extrinsic ones (the three Euler angles α , β and γ), and the translation vector $(T_x, T_y, 0)'$ of a fixed zoom and focus videomicroscope. The linear model of the video microscope is simplified by considering a single scale factor instead of two, and the concept of a multiple scale model is introduced by representing this scale factor as a function of the magnification. This idea is similar to the one proposed by Tarabani *et al.* [5] and Sturm [6] in the case of a macroscopic zoom-lens camera system. The multiple scale paradigm is introduced for the manipulation of MEMS by means of visual control, approach that is particularly relevant for the robotic handling of MEMS (e.g. grabbing or picking up). The authors describe as well the concepts required to perform the assembly of simple MEMS in order to build 3D solid and complex MEMS (up to five microparts are assembled). Microparts are tracked by computing their 3D pose in the frame of a videomicroscope using a 3D tracking based-model. A pose-based visual servoing is developed and validated by some microassembly of silicon microparts. The proposed experimental setup includes a motor zoom photon videomicroscope watching the work scene vertically, a manual zoom photon videomicroscope tilted at 45° with respect to the horizontal plane, a five dof microrobotic system (a two-finger gripper, a manipulator and a mobile platform). The authors also discuss the multi scale modeling of the motor zoom microscope, the corresponding image-based visual control implemented for the manipulation of MEMS and the assembly of MEMS by the pose-based control using the images of the manual zoom videomicroscope tilted at 45° from the vertical axis.

2. Multiscale Model

The components of any photon image source are a video lens in association with a camera. The first component focuses the rays into the surface of the sensor (camera) which converts the photonic energy into an electric energy. According to the video lens, three types of image sources can be considered. The basic image source is the pinhole camera, where no conventional lens model is used. An extremely small hole in a very thin material focuses light by confining all the rays from the scene. In order to produce a reasonably clear image, the aperture has to be about a hundred times smaller than the distance to the sensor, or less. The standard image source is more complicated than the pinhole

camera; it includes a standard video lens whose focal length is greater than some millimeters. The optical magnification is very small and the resolution is consequently very weak. Image formation on the sensor is driven by standard geometrical and physical optics. The final type of photon image source is the videomicroscope whose rays are focused by means of a microscope. The modern compound microscope is designed to provide a magnified two-dimensional image which is focused axially in successive focal planes. It is equipped with infinity-corrected objectives, which are responsible for primary image formation and play a central role in determining the quality of the image. The focal length of the microscope is smaller than a millimeter. In some cases, a tube is also associated in order to increase the magnification.

2.1. Basic Model

Standard lens based image source is modeled by the non-linear projective model. The latter includes:

- Intrinsic parameters inherent to the imaging system: the focal length f , the scale factors k_x and k_y in x and y directions, the principal point coordinates (x_o, y_o) (front focal point)
- Extrinsic parameters corresponding to the position and orientation of the camera frame with respect to the scene frame: translation components T_x, T_y and T_z and the Euler angles α, β , and γ
- Distortion parameters including the radial $(a_1, a_2 \dots)$ and tangential $(b_1, b_2 \dots)$ distortion coefficients.

The improvement of technology enables the manufacturing of isotropic image sensors in which the scale factors along x and y are identical:

$$k_x = k_y = k \quad (1)$$

The microscope based image source is an optical imaging and can thus be modeled by the non-linear projective model. However, the quality of laboratory microscope is usually better than that of standard lens. Experimental values of distortion parameters are very weak: ranging from 10^{-8} to 10^{-10} [3, 7]. Therefore, the distortions can be neglected, and the linear projective model can be used to modelize the videomicroscope. The model consists of a perspective projection of a scene point P onto a pixel p in the retinal plane through the optical centre. Let P and p be respectively represented by the homogeneous vector $(X, Y, Z, I)'$ and $(x, y, w)'$, then:

$$p = QP \quad (2)$$

The matrix Q , of dimension 3×4 , is the homogeneous projection matrix of the image source:

$$Q = K \begin{bmatrix} 1 & 0 & 0 & 0 \\ 0 & 1 & 0 & 0 \\ 0 & 0 & 1 & 0 \end{bmatrix} * D \quad (3)$$

The matrix K gathers the intrinsic parameters:

$$K = \begin{pmatrix} fk & 0 & x_0 \\ 0 & fk & y_0 \\ 0 & 0 & 1 \end{pmatrix} \quad (4)$$

In the microscopes where a tube is associated with the lens, the parameter f in Eq. (4) is the sum of the focal length with the length of the tube. The displacement matrix D combines the rotation matrix R of dimension (3×3) and the translation vector T of dimension (1×3) :

$$D = \begin{pmatrix} R_{3 \times 3} & T_{1 \times 3} \\ 0 & 1 \end{pmatrix} \quad (5)$$

If the Euler angles α , β , and γ are considered, the rotation matrix is:

$$R = \begin{pmatrix} \cos \alpha \cos \beta & \cos \alpha \sin \beta \sin \gamma - \sin \alpha \cos \gamma & \cos \alpha \sin \beta \sin \gamma + \sin \alpha \sin \gamma \\ \sin \alpha \cos \beta & \sin \alpha \sin \beta \sin \gamma + \cos \alpha \cos \gamma & \sin \alpha \sin \beta \cos \gamma - \cos \alpha \sin \gamma \\ -\sin \beta & \cos \beta \sin \gamma & \cos \beta \cos \gamma \end{pmatrix} \quad (6)$$

2.2. Multiscale Model

Multiscale calibration is required because the videomicroscope considered in the experiments works at multiple zoom position or magnification, and it is necessary to introduce the zoom factor ζ in the previous intrinsic model. The solution adopted in this paper is to consider only the scale factor k as a non-linear function of the zoom factor ζ : $k=k(\zeta)$. When it is assumed that the others parameters are not modified by the zoom factor:

$$K = \begin{pmatrix} fk(\zeta) & 0 & x_0 \\ 0 & fk(\zeta) & y_0 \\ 0 & 0 & 1 \end{pmatrix} \quad (7)$$

Consequently, the knowledge of the zoom factor ζ permits an estimation of the focal length:

$$f = \frac{K_{11}}{k(\zeta)} \quad (8)$$

where $K_{11} = fk$ is the first element of the calibration matrix K . More details about this method are available in [8].

3. Multiscale Image-Based Visual Servoing for MEMS Micromanipulation

When several degrees of freedom have to be controlled, the visual servoing is achieved using an exponential decrease of the task function as presented in Chaumette *et al.* [9, 10]. The multiple scale paradigms are introduced by explicitly modeling the scale factor and the focal length as functions of the magnification or zoom factor [11]. A similar solution (multiple scale visual servoing) is developed in Devanathan *et al* [12]. It consists in combining two loops: a feedback from a macroscopic view (standard scope) to focus in the area of interest and a feedback from a microscopic view to actually perform the MEMS handling. Unlike this approach where the authors use two imaging systems to associate the global view to the local view of the scene, we propose a new approach where only one imaging system (videomicroscope equipped with variable and controlled zoom and focus) is used to perform a multiple scale visual servo.

The multiscale calibration performed links the scale factor k with the zoom factor ζ according to the following polynomial relation:

$$k = [c_1, c_2 \dots c_{11}] [\zeta^{10}, \zeta^9, \dots, 1]' \quad (9)$$

$(c_1, c_2 \dots c_{11})$ are the polynomial coefficients. Consequently, the focal length (f) and the feature points $s(\zeta)$ are functions of the zoom factor (ζ). Let $s(\zeta)$ and $s^*(\zeta)$ be the current and desired value of the set of selected visual feature points, respectively. The velocities (\dot{s}) of those visual features are linked to the relative velocity of the camera/scene, v , by the following equation:

$$\dot{s} = L_s(s, Z_f, \zeta)v \quad (10)$$

where L_s is the interaction matrix and (v) , the kinematic screw, is given by the following formula:

$$v = (v_x, v_y, v_z, w_x, w_y, w_z) \quad (11)$$

and Z_f represents the depth information of the object expressed in the camera frame. A depth-from-focus approach computes this information [11]. Then the interaction matrix for the coordinates x and y can be written as:

$$L_s(x, y, Z_f, \zeta) = \begin{pmatrix} \frac{-1}{Z_f} & 0 & \frac{x(\zeta)}{Z_f} & x(\zeta)y(\zeta) & -1 - x(\zeta)^2 & y(\zeta) \\ 0 & \frac{-1}{Z_f} & \frac{y(\zeta)}{Z_f} & 1 + y(\zeta)^2 & -x(\zeta)y(\zeta) & -x(\zeta) \end{pmatrix} \quad (12)$$

Let e be the error between the current position $s(\zeta)$ and the desired position $s^*(\zeta)$.

$$e = s(\zeta) - s^*(\zeta) \quad (13)$$

Considering an exponential decrease of the error, we have:

$$\dot{e} = -\lambda e \quad (14)$$

That leads to the following control law:

$$v = -\lambda \hat{L}_s e \quad (15)$$

where λ is a positive gain. For a better convergence (good speed and without overshoot) of \dot{e} , the gain is adapted to the value of e according to the following formula:

$$\lambda = (\lambda_{\max} - \lambda_{\min}) \exp^{-\rho \|e\|} + \lambda_{\min} \quad (16)$$

where λ_{\max} and λ_{\min} are respectively the maximum and minimum values of λ . The parameter ρ allows the tuning of the decreasing rate of the error exponential decrease.

This visual servoing approach can be represented by the functional chart shown in Fig. 1.

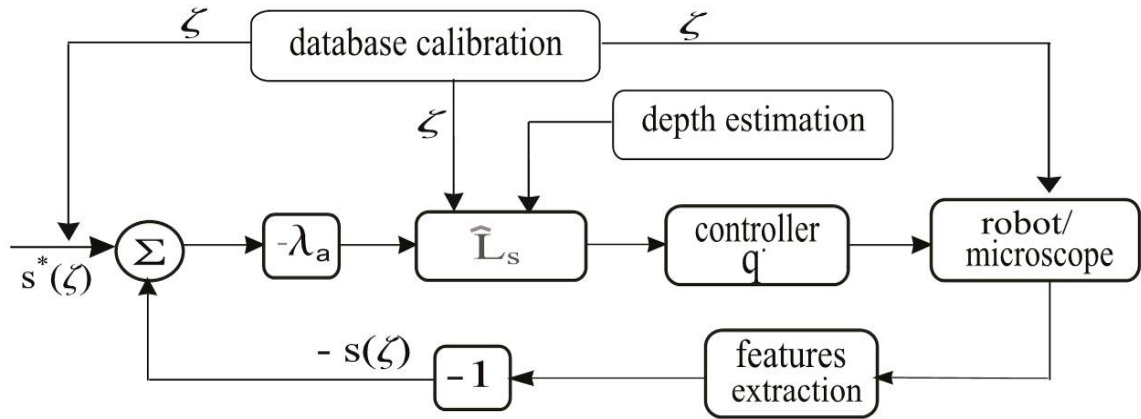


Fig. 1. The function chart of multiple scale image-based visual servoing.

4. Pose-Based Visual Control for MEMS Microassembly

Microassembly is a delicate operation because in addition to the stages of MEMS handling described in the previous section, it requires a much more complicated task which is an insertion task. The latter represents the fitting together of two or more simple MEMS in order to build 3D solid MEMS. This task requires the control of the position and orientation in space of the involved microparts. In this case, image-based visual control (or 2D visual servoing) is not relevant when pose-based visual control (also known as 3D visual control) is natural and relevant to perform that task.

MEMS robotic assembly has been well studied in the literature [1, 2, 13, 14, 15, 16]. In most cases, image-based visual servoing solutions were implemented. However the latter have shown some incontrovertible limits: the weakness of the field-of-view of the photon videomicroscope, the occlusion of the field by the robotic components and especially the ambiguity of MEMS position and orientation because of the 2D dimension of the images. Pose-based visual control appears to be the convenient solution to the issue of MEMS assembly. By implementing together a 3D tracking by CAD (Computer-Aided Design) models and control of targets, a solution is obtained which resolves the problem of ambiguity: the resolvability of the imaging system is increased as demonstrated by Nelson [13]. The impact of occlusions is reduced also since the 3D tracking is robust to occlusions. Except the papers of Feddema *et al.* [14] and Yesin *et al.* [13], no publication has never really implemented the assembly of MEMS by means of CAD model-based tracking and control. The law control presented in these papers is of the type 3D *look and move*. As opposed to these works, we developed a control law using a form of 3D interaction matrix which is faster and more stable compare to the *look and move* approach.

Let us consider the example of an assembly task of five simple MEMS {A, B, C, D and E} to build a complex and solid 3D MEMS as illustrated by Fig. 2. The insertion tolerance of two microparts is less than $3 \mu m$. The precision criterion is of great importance in the approach as well as the time required to complete the full assembly.

Fig. 3 shows the 3D positions of the different frames: R_A, R_B, R_C, R_D and R_E linked to each MEMS.

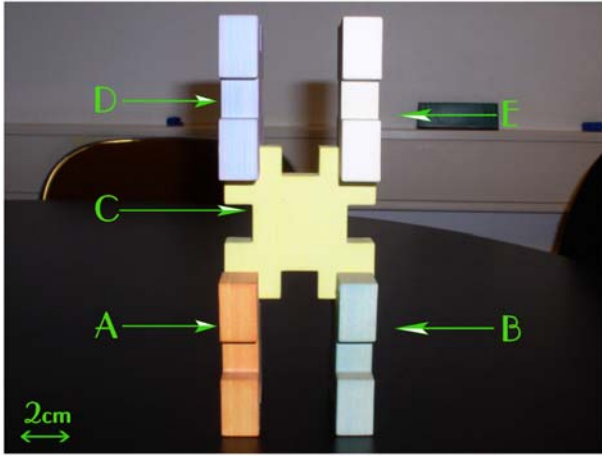


Fig. 2. An assembly operation for macroparts.

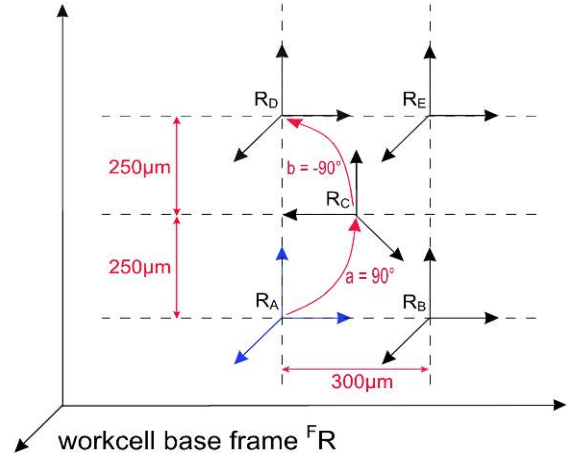


Fig. 3. Desired positions of each micropart to assemble.

Let us define, for example, the rigid transformation between a frame R_i and a frame R_j by a homogenous matrix iM_j defined as:

$${}^iM_j = \begin{pmatrix} {}^iR_j & {}^it_j \\ 0 & 1 \end{pmatrix} \quad (17)$$

where iR_j is the rotation matrix and it_j the translation vector. It is also possible to note the pose by the vector ir_j , (Eq. 18). A tracking algorithm Visual Servoing Platform (VISP) developed by Marchand *et al.* [16], [17] is used to compute the 3D poses of microparts tracked at real-time.

$${}^ir_j = ({}^it_j, \theta u), \quad (18)$$

where θu is the axes and the angle of the rotation.

The equation that links the variation \dot{s} of the visual feature s to the robot velocity in the robot reference frame $(v, w)_F^T$ are given by:

$$\begin{pmatrix} {}^F\dot{t}_{np} \\ \dot{\theta}u \end{pmatrix} = \begin{pmatrix} I_{3 \times 3} & 0_{3 \times 3} \\ 0_{3 \times 3} & J_w \end{pmatrix} = \begin{pmatrix} v \\ w \end{pmatrix}_F \quad (19)$$

with:

$$J_w = L_w^{np} R_F \quad (20)$$

where $\{np\}$ is the micro-object label and L_w is such that:

$$L_w^{-1} \theta u = \theta u \quad (21)$$

We finally obtain the following control law:

$$\begin{pmatrix} \mathbf{v} \\ \mathbf{w} \end{pmatrix}_F = -\lambda \begin{pmatrix} \mathbf{I}_{3 \times 3} & \mathbf{0}_{3 \times 3} \\ \mathbf{0}_{3 \times 3} & \mathbf{J}_w^{-1} \end{pmatrix} (\mathbf{s} - \mathbf{s}^*) \quad (22)$$

$$= -\lambda \begin{pmatrix} {}^F \mathbf{t}_{np} & -{}^F \mathbf{t}_{np}^* \\ {}^F \mathbf{R}_{np} & \theta \mathbf{u} \end{pmatrix} \quad (23)$$

The robotic system presented in this paper includes two separate systems: a positioning platform and a micromanipulator. For the positioning platform, we control three dof ($xy\theta$) and the control law corresponding to this task is obtained by simplifying the previous relationship:

$$\begin{pmatrix} \dot{x} \\ \dot{y} \\ \dot{\theta} \end{pmatrix}_F = -\lambda \begin{pmatrix} t_x - t_x^* \\ t_y - t_y^* \\ {}^F \mathbf{R}_{np} \theta \mathbf{u}_\theta \end{pmatrix} \quad (24)$$

In the same way, the control law defined in (25) ensures the control of the two dof ($z\phi$) of the micromanipulator:

$$\begin{pmatrix} \dot{z} \\ \dot{\phi} \end{pmatrix} = -\lambda \begin{pmatrix} t_z - t_z^* \\ {}^F \mathbf{R}_{np} \theta \mathbf{u}_\phi \end{pmatrix} \quad (25)$$

Fig. 4 shows the corresponding chart of this approach in the case of two simple MEMS. The MEMS {A} and {B} are tracked by their CAD models and the robotic system is controlled by means of pose-based visual servo in order to achieve the insertion of {B} into {A}. It should be stressed that the positioning task of the different microparts between the end-effectors and the gripping of the micropart task are achieved by means of previous image-based visual servo.

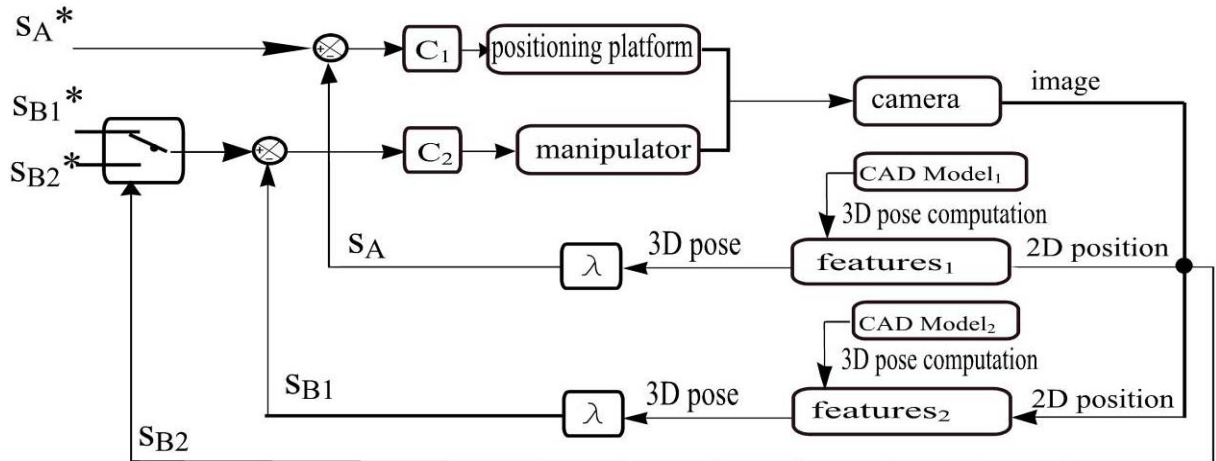


Fig. 4. Function chart of the insertion by means of dual 3D visual control.

The switching between the different 3D desired poses of the microparts on the 3D structure is computed automatically by the following relationship:

$${}^F \mathbf{M}_l = \mathbf{M}_0 * \mathbf{M}_m^n, \quad (26)$$

where l ($l = \{A, B, C, D \text{ and } E\}$) is the micro-object label and M_0 represents the desired position of the first micropart $\{A\}$ which is defined manually. M_m^n is the passage matrix between the desired position of micropart $\{n\}$ and micropart $\{m\}$.

The switch between the different tasks of positioning (control of the positioning platform) and insertion (control of the micromanipulator) for successive microparts is done when the threshold of translation and rotation error is reached ($[e_t < 1\mu m]$ and $[e_r < 0.5^\circ]$). The same threshold is applied for all the tasks.

The desired position of the first micropart $\{A\}$ is defined manually (${}^F M_A$) (Initialization step). When $\{A\}$ is perfectly positioned ($[e_t < 1\mu m]$ and $[e_r < 0.5^\circ]$), the final position of the second micropart is computed automatically using Eq. (25). A translation of $300 \mu m$ along the z axis is made from the pose of the micropart $\{A\}$. The matrix passage ${}^F M_A^B$ between the final pose $\{A\}$ and the final pose $\{B\}$ is given by the following formula:

$${}^F M_A^B = \begin{pmatrix} 1 & 0 & 0 & 0 \\ 0 & 1 & 0 & 0 \\ 0 & 0 & 1 & 300 \\ 0 & 0 & 0 & 1 \end{pmatrix} \quad (27)$$

The sequence is repeated for the desired position of micropart $\{B\}$ and $\{C\}$ using Eq. (28). It includes a rotation of $\alpha = 90^\circ$ around the vertical axis z , a translation of $-250 \mu m$ along y and $150 \mu m$ along x .

$${}^F M_A^C = \begin{pmatrix} 0 & 0 & 1 & 0 \\ 0 & 1 & 0 & -250 \\ -1 & 0 & 0 & 150 \\ 0 & 0 & 0 & 1 \end{pmatrix} \quad (28)$$

The transformation between the final position of the micropart $\{A\}$ and the fourth micropart $\{D\}$ is given by the following relationship:

$${}^F M_A^D = \begin{pmatrix} 1 & 0 & 0 & 0 \\ 0 & 1 & 0 & -500 \\ 0 & 0 & 1 & 0 \\ 0 & 0 & 0 & 1 \end{pmatrix} \quad (29)$$

The last desired pose corresponding to micropart $\{E\}$ is given by the rigid transformation in Eq. (30). It consists of two translations of $-250 \mu m$ and $-500 \mu m$ respectively along x and y .

$${}^F M_A^E = \begin{pmatrix} 1 & 0 & 0 & -250 \\ 0 & 1 & 0 & -500 \\ 0 & 0 & 1 & 0 \\ 0 & 0 & 0 & 1 \end{pmatrix} \quad (30)$$

5. Experimental Setup

To validate the approaches and concepts proposed in this paper, a microassembly workcell was designed, as shown in Fig. 5. From a mechanical point of view, the station consists of five dof: three dof are dedicated to the positioning platform (two linear stages xy and one rotating stage θ), the second part is a micromanipulator equipped with two dof (one vertical linear stage z and one rotating stage φ tilted at 45° from the vertical one). The micromanipulator supports four dof ($y_1y_2z_1z_2$) gripping system which consists in a piezoelectric driven two-finger gripper. A detailed description of this gripper can be found in [18]. An optical videomicroscope equipped with a computer controlled zoom and focus (MZ16A from Leica) is used for the multiple scale image-based visual control. The magnification ranges from $0.71\times$ to $11.5\times$. The minimum field-of-view is $700\ \mu\text{m} \times 900\ \mu\text{m}$. The depth-of-field varies between $0.035\ \text{mm}$ and $2.9\ \text{mm}$. Another monochrome optical videomicroscope (Navitar zoom 6000 with $1\times$ adaptor and a CCD camera) is used to perform the MEMS assembly using the pose-based visual servoing presented in section 4. Its characteristics are $4.5\times$ magnification, a depth-of-field of $0.09\ \text{mm}$. The vision system (optical videomicroscope) is tilted at 45° from the work frame. This configuration is chosen in order to improve the perspective view of the MEMS during the various steps of assembly.

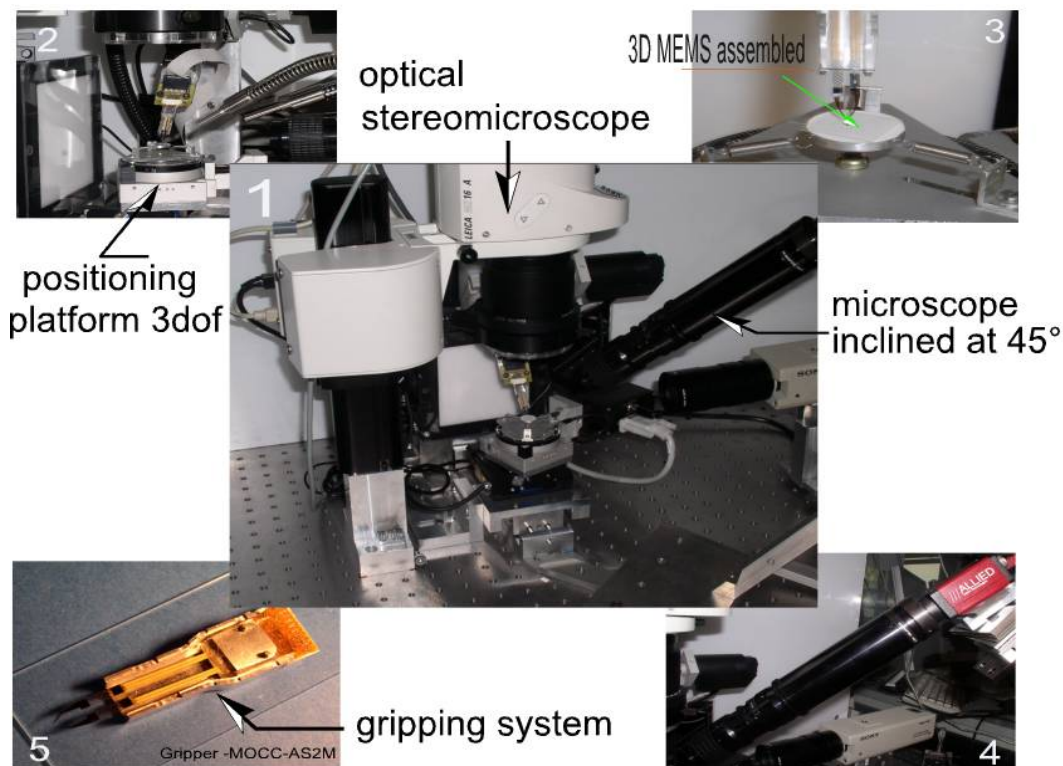


Fig. 5. Global and local views of each part (positioning platform, the compliant support of the micro-objects, the gripping system and the imaging system) of the assembly workcell.

6. Experimental Results

6.1. Multiscale Calibration Results

As a consequence of the weakness of the depth-of-field, a 3D calibration sample cannot be used; the sample is reduced to a planar object that should be almost parallel to the lens. A videomicroscope is

heavy and cumbersome and is thus not easy to manipulate. These constraints complicate the calibration. On the other hand, the presence in the set-up of accurate motion sources as xyz stages enables the performing of accurate motions of the plane calibration sample and contributes to facilitate the calibration.

Instead of using a real sample [3] or virtual points [7] as encountered in the literature, we use the power of image processing (auto-correlation algorithm): the centre of a micrometric micropart is tracked in the images of the scene, as depicted in Fig. 6. The micropart is moved accurately by a xyz stage, so its central position in the scene is known with high accuracy. These positions are used to synthesize a virtual image which is used in the algorithm presented before. This approach enables a high accuracy in the computing of the model parameters. The approach is also simple, since it does not require the micromachining of any pattern. The components to assemble are directly used.

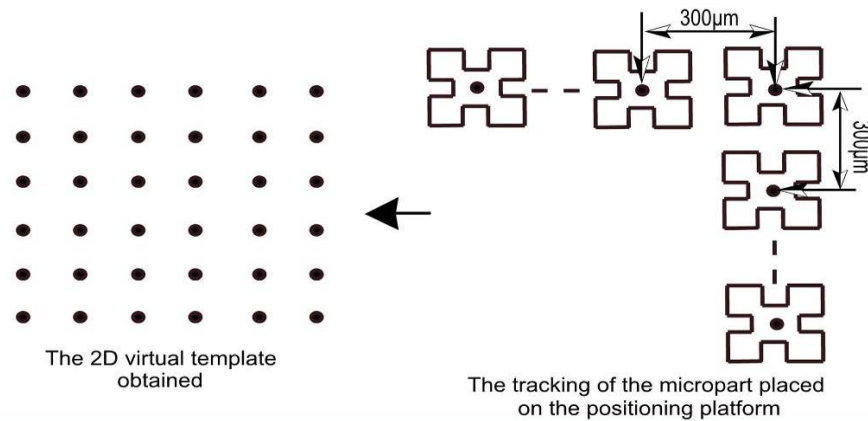


Fig. 6. Virtual pattern construction method using image processing algorithm based on an auto-correlation detection of the silicon micropart manipulated.

Fig. 6 shows steps of x and y displacements of $300\mu\text{m}$ performed for the generation of the 2D virtual pattern used to calibrate the imaging system. Fig. 7 represents the evolution of the scale factor $k(\zeta)$ according to the zoom factor (ζ). The approximation of this function by a polynomial function using MatLab gives a polynomial P of degree ten.

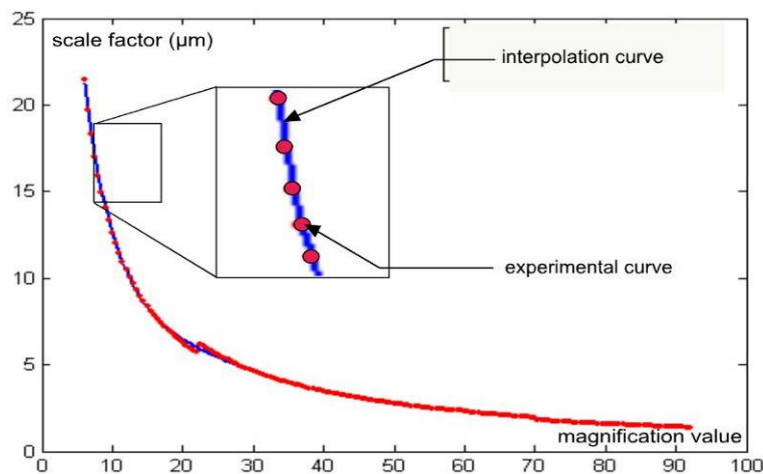


Fig. 7. Scale factor according to zoom factor.

For a zoom position of $38\times$, the computation of the calibration matrix gives:

$$K = \begin{pmatrix} 3146.3 & 0 & 512.5 \\ 0 & 3146.3 & 385.5 \\ 0 & 0 & 1 \end{pmatrix} (pixels) \quad (31)$$

According to the equations, the following values are extracted:

$$\begin{aligned} k &= k_x = k_y = 3.6444 \mu m \\ f &= 11.466 \times 10^3 \mu m \end{aligned} \quad (32)$$

and the extrinsic parameters are:

$$\begin{cases} \alpha = 88.73^\circ \\ \beta = -27.26^\circ \\ \gamma = 4.01^\circ \\ T_v = [822 \quad 963 \quad 13156]' mm \end{cases} \quad (33)$$

6.2. MEMS Micromanipulation Results and Discussions

The multiple scale image-based visual servoing presented in section 3 is validated by a basic micromanipulation task which consists in a pick and place of silicon microparts of $400\mu m \times 400\mu m \times 100\mu m$. The pick and place cycle is decomposed in subtasks such as: detection of the micropart, aligning + increasing the scale, positioning (between the gripper end-effectors) + increasing the scale, centering + increasing the scale, opening the gripper, descent of the gripper, closing the gripper, ascent of the gripper with the micropart + decreasing the scale, transfer of the micropart to the target + decreasing the scale, descent of the gripper + decreasing the scale, release of the micropart + decreasing the scale and the cycle is ended by a return of the gripper to the original location. Several pick and place cycles are performed with different configurations of the initial position of the micropart. The results obtained are presented for different points:

- A success rate for several pick and place cyclic has been calculated (72% of success)
- The robustness of partial occlusions of the micropart tracked during the control is proven
- A high x positioning accuracy is obtained ($\sim 1.4 \mu m$), such quality precision of the orientation is obtained ($\sim 0.5^\circ$)
- The good convergence (without overshoot) of the control law (multiple scale visual servoing) is ensured using the adaptive gain in Eq. (16)

Fig. 8 illustrates the sequence of the basic tasks executed using the developed visual servoing. Fig. 8.1 shows the initial position of the micropart, Fig. 8.2 shows the micropart alignment task, and Fig.8.3-8.5 illustrate the positioning task + increasing scale. The image sequence is ended with a centering task of the micropart between the gripper end-effectors for gripping task. The gripping operation on the micro-object is controlled using the vision sensor, as the gripper is not equipped with a force sensor yet. It consists in a 2D tracking of the gripping tips and a *look and move* control is developed to ensure the gripping task.

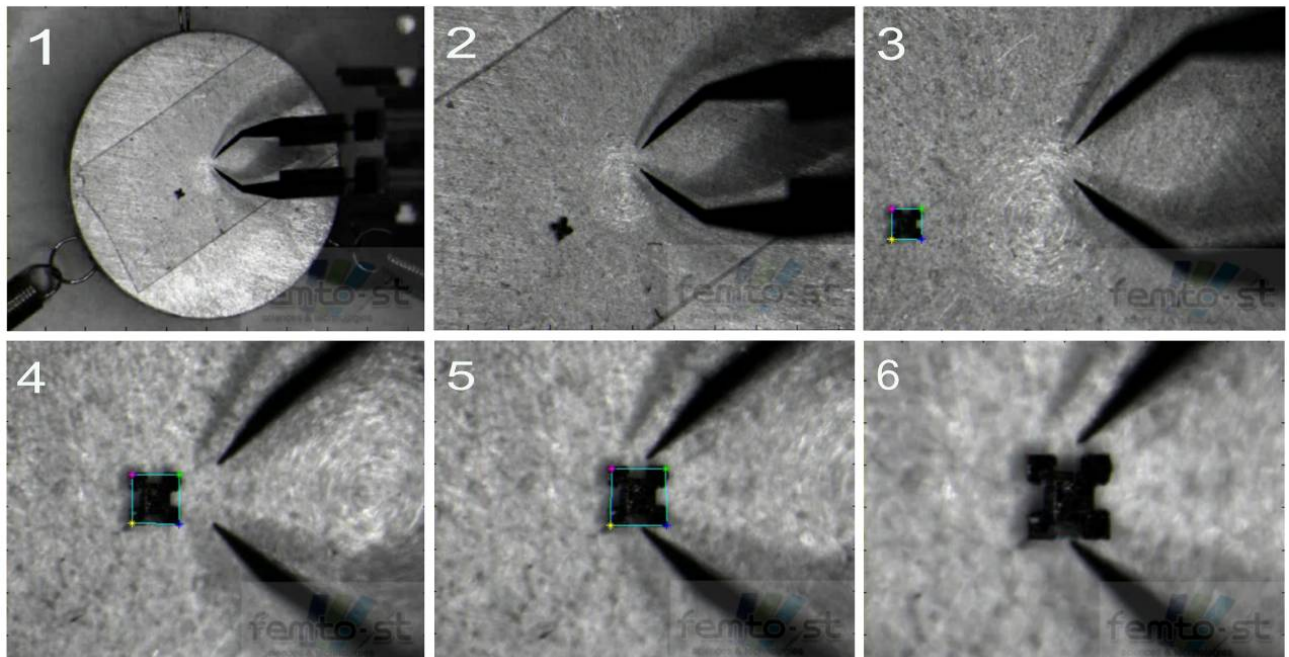


Fig. 8. Several shots during the studied sequence (detection, alignment, positioning and cantering).

Fig. 9 shows several results of different automatic micromanipulation of silicon micropart, metal microball and optical microfiber. Fig. 9.1 and 9.2 show the respective side views of a metal microball of $200\ \mu\text{m}$ diameter and a square silicon micropart of $400\ \mu\text{m} \times 400\ \mu\text{m} \times 100\ \mu\text{m}$ handled using the multiscale image-based visual control. Fig. 9.3 illustrates micromanipulation of an optical microfiber of $125\ \mu\text{m}$ of diameter using the same control law.

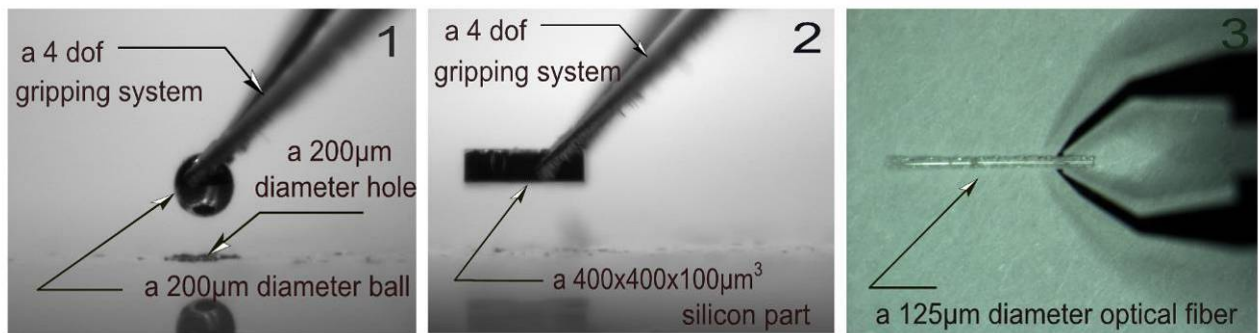


Fig. 9. Examples of different microparts (metal ball, square silicon micropart, optical fiber) used to validate the concepts and approaches proposed above.

6.3. MEMS Microassembly Results and Discussions

In this subsection, we show that the microassembly MEMS is possible using a 3D visual control associated to a high precision CAD model-based tracking. It has been proven in the previous sections that the complex assembly illustrated in Fig.10 is impossible to be achieved in tele-operation mode (with a joystick), even with a human operator with enough experience in tele-operated handling. Therefore, an automatic approach is more efficient. Promising results are obtained, especially in terms of accuracy, robustness, repeatability and the time required to achieve a full assembly (~ 40 seconds to perform positioning and insertion of two micro-objects). The mean positioning error (translation) is

less than $2.04\ \mu\text{m}$ and the mean orientation error (angular) is less than 0.48° . The high quality of the results allows performing MEMS assemblies with an insertion tolerance (mechanical play) less than $3\ \mu\text{m}$. Therefore, solid MEMS can be assembled without any external joining (glue or welding).

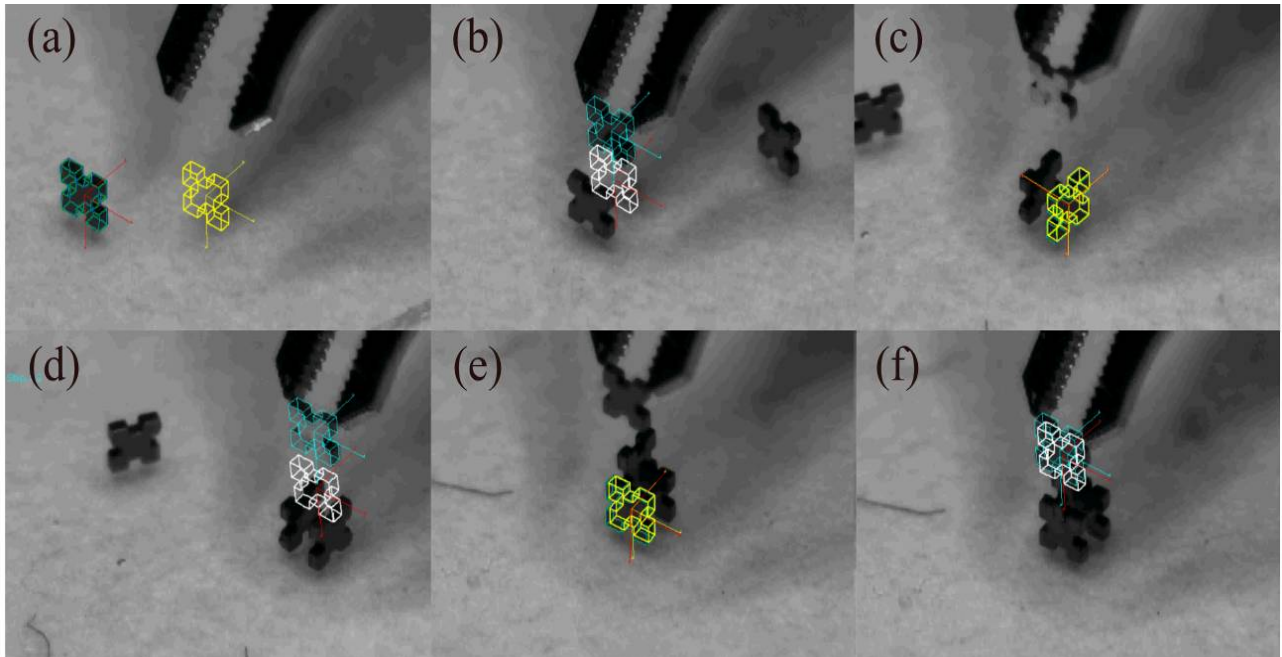


Fig. 10. Sequence of images taken during the assembly process.

Fig. 10 represents a sequence of images from the optical videomicroscope system showing the process of the automatic microassembly of five silicon microparts of size of $400\mu\text{m} \times 400\mu\text{m} \times 100\mu\text{m}$. Fig. 10a illustrates the first step which concerns the tracking and the positioning of the micropart {A}. Fig. 10b presents the tracking and placing of the micropart {B}. Fig. 10c shows the tracking and the positioning of the both microparts {[A+B]}, while Fig. 10d depicts the tracking and insertion of the micropart {C} into the micropart {[A+B]}. Fig. 10e presents the tracking of the micropart {A} and the positioning of the microparts {[A+B+C]}. Fig. 10f depicts the tracking and the insertion of the micropart {D} into the microparts {[A+B+C]}. Finally, Fig. 11 illustrates the solid and complex 3D microassembly performed.

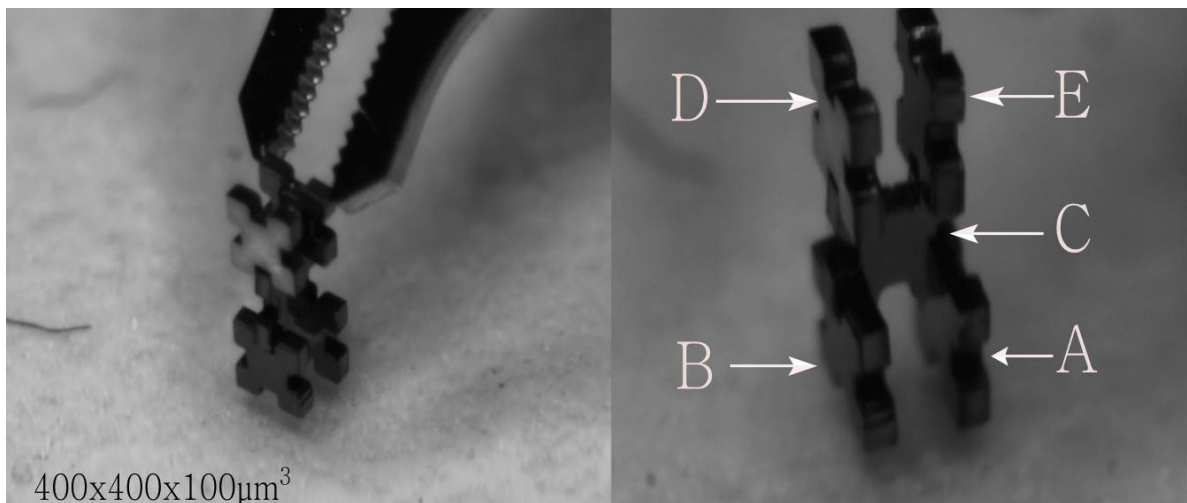


Fig. 11. Images of the solid and complex 3D microassembly (five microparts, 3 levels) obtained.

7. Conclusions

The robotic microassembly task is the assembly of micrometric (submillimeter) parts to works multicomponents products by means of a robotic system in conjunction with a gripping system and an imaging system. When the imaging system delivers images from which a lot of information can be extracted, the problem is that high resolution (local view) and low resolution (global view) information must be caught at the same time. An interesting solution to the problem is the multiple scale imaging using a photon videomicroscope equipped with a tunable zoom. This paper deals with the multiscale modelling of the variable zoom of the photon videomicroscope as well as the manipulation and assembly of MEMS by means of visual control (image and pose-based).

It was shown that the functioning of controllable zoom videomicroscope can reasonably be described by a simplified projective model. The first simplification is relative to the omission of distortions because of the weak values of their coefficients. The second simplification consists in considering that the scale factor along the axis x and y is equal. Finally the (intrinsic) parameters become the focal length f , the scale factor k , the principal point coordinates (x_o, y_o) . The concept of multiple scale modelling is introduced through the zoom factor ζ whose mathematical relation with the scale factor k is claimed: k is a polynomial of ζ . The following approach of calibration is proposed: the polynomial $k(\zeta)$ is accurately estimated by changing the zoom factor ζ and computing the corresponding scale factor k . The linear projective model is computed using a usual calibration approach with a virtual calibration sample. The calibration results are used to perform robotic MEMS manipulation by means of image-based visual control and assembly by means of pose-based visual control. The multiple scale image-visual servoing achieves a pick and place including basic tasks like aligning, positioning, centring, and gripping. The results prove the relevance of the concepts. A 72% success rate of the different pick and place performed is obtained. Indeed, the failure rate of 28% is mainly the results of physical phenomena (adhesion forces) and hardly a consequence of control error or occlusions.

The MEMS assembly (assembly of five silicon microparts) is performed by a pose-based visual control. It was shown that the precision obtained during the experimental validation of this approach is good and it is sufficient to consider assembling solid and complex MEMS without external solidarization such as gluing or welding. This accuracy is less than $2.08 \mu m$ along the translation motions and 0.48° for the orientation motions. The automation of MEMS assembly using a visual sensor feedback permits assembly tasks which was impossible to achieve in teleoperating mode for a human operator. In addition, the time required for MEMS assembly is divided by 15 by this automatic approach developed.

Acknowledgements

This work is partially conducted with financial support from the project Hybrid Ultra Precision Manufacturing Process Based on Positional and Self assembly for Complex Micro-Products (HYDROMEL NMP2-CT-2006-026622) funded by the European Commission.

References

- [1]. W. T. Sun and T. C. Chin, Image-based visual servo for micromanipulation a multiple-view and multiple-scale approach, *International Symposium on Micro-Nanomechatronics and Human Science*, November 2004, pp. 341-346.

- [2]. S. Ralis, B. Vikramaditya, and B. J. Nelson, Micropositioning of a weakly calibrated microassembly system using coarse-to-fine visual servoing strategies, *IEEE Transactions on Electronics Packaging Manufacturing* Vol. 23, Issue 2, 2000, pp. 123-131.
- [3]. Y. Zhou and B. J. Nelson, Calibration of a parametric model of an optical microscope, *Optical Engineering*, Vol. 38, No. 12, 1999, pp. 1989-1995.
- [4]. R. Y. Tsai, A versatile camera calibration technique for high-accuracy 3d machine vision metrology using off-the-shelf TV cameras and lenses, *IEEE Journal of Robotics and Automation*, Vol. RA-3, No. 4, 1987, pp. 323-344.
- [5]. K. Tarabani, R. Y. Tsai, and D. S. Goodman, Calibration of a computer controlled robotic vision sensor with zoom lens, *CVGIP*, Vol. 59, Issue 2, March 1994, pp. 226-241.
- [6]. P. Sturn, *Self-calibration of a moving zoom-lens camera by precalibration*, *IVC*, Vol. 15, Issue 08, 1997, pp. 583-589.
- [7]. M. Ammi, V. Fremont, and A. Ferreira, Flexible microscope calibration using virtual pattern for 3-d telemicromanipulation, *IEEE International Conference on Robotics and Automation*, April 2005, pp. 3888-3893.
- [8]. B. Tamadazte, S. Dembélé, and N. Le Fort-Piat, A multiscale calibration of a photon video microscope for visual servo control: Application to micromanipulation, *IEEE International Workshop on Robotic and Sensors Environments*, Ottawa, Canada, October 2008, pp. 29-34.
- [9]. F. Chaumette and S. Hutchinson, Visual servo control, part 1: Basic approaches, *IEEE Robotics and Automation Magazine*, Vol. 13, No. 4, 2006, pp. 82-90.
- [10]. B. Espiau, F. Chaumette, and P. Rives, A new approach to visual servoing in robotics, *IEEE Transactions on Robotics and Automation*, Vol. 8, Issue 3, 1992, pp. 313-326.
- [11]. B. Tamadazte, S. Dembélé, G. Fortier, and N. Le Fort-Piat, Automatic micromanipulation using multiscale visual servoing, *IEEE Conference on Automation Science and Engineering*, Washington, USA, August 2008, pp. 977-982.
- [12]. R. Devanathan, S. Wenting, C. T. Chai and A. Schacklock. Multi View and Multi Scale Image Based Visual Servo For Micromanipulation, *Studies in Computational Intelligence*, Vol. 8, 2005, pp. 105-133.
- [13]. K. Berk Yesin and B. J. Nelson, Robust cad model-based visual tracking for 3d microassembly using image space potentials, *IEEE International Conference on Robotics and Automation*, New Orleans, USA, April 2004, pp. 1868-1873.
- [14]. John T. Feddema and Ronald W. Simon, Visual servoing and CAD-driven microassembly, *IEEE Robotics and Automation Magazine*, Vol. 5, Issue 4, 1998, pp. 18-24.
- [15]. D. O. Popa and H. E. Stephanou, Micro and mesoscale robotic assembly, *Journal of Manufacturing Process*, Vol. 6, Issue 1, 2004, pp. 52-71.
- [16]. E. Marchand, F. Spindler, and F. Chaumette, ViSP for visual servoing : a generic software platform with a wide class of robot control skills, *IEEE Robotics and Automation Magazine*, Vol. 12, No. 4, 2005, pp. 40-52, Special Issue on "Software Packages for Vision-Based Control of Motion", P. Oh, D. Burschka (Eds.).
- [17]. A. I. Comport, E. Marchand, M. Pressigout, and F. Chaumette, Real-time markerless tracking for augmented reality: the virtual visual servoing framework, *IEEE Transactions on Visualization and Computer Graphics*, Vol. 12, No. 4, 2006, pp. 615-628.
- [18]. J. Agnus, P. Nectoux, and N. Chaillet, Overview of microgrippers and design of a micromanipulation station based on MMOC microgripper, *IEEE International Symposium on Computational Intelligence in Robotics and Automation*, Finland, 2005, pp. 117-123.